

Supporting Information for “Electron transport in crystalline PCBM-like fullerene derivatives: a comparative computational study”

Julien Idé, Daniele Fazzi, Mosè Casalegno, Stefano V. Meille, Guido Raos

June 6, 2014

1 Adiabatic and non-adiabatic free energy barriers

In the non-adiabatic (na) approximation, the coupling between the initial and final electronic states involved in an electron transfer (ET) reaction is neglected (weak coupling approximation), so that the free energy barrier of the reaction is determined from the initial and final non-interacting diabatic states. In the case of a non-symmetrical ET reaction, as illustrated in figure S1, the diabatic potential energy surfaces of the initial and final states can be approximated by the parabolic functions:

$$V_i(q) = 1/2f(q - q_i)^2 \quad (1)$$

$$V_f(q) = 1/2f(q - q_f)^2 + \Delta E_{if} \quad (2)$$

where q_i and q_f denote the value of the reaction coordinate at the initial and final states, i.e. to the system geometry before and after ET. f is the curvature of the two parabolas (assumed for simplicity to have identical values in the two states) and ΔE_{if} the energy difference between the final and initial states at their equilibrium geometries. The crossing point of the two parabolas ($q = q_c$) is determined by the condition of equality of the two potential energy curves:

$$q_c = \frac{\Delta E_{if}}{f} \left(\frac{1}{q_f - q_i} \right) + (q_f + q_i) / 2. \quad (3)$$

Taking the energy origin at the minimum of the initial state parabola, the non-adiabatic free energy barrier can be written as:

$$\Delta E_{na}^\ddagger = V_i(q_c) - V_i(q_i) = 1/2f(q_c - q_i)^2 \quad (4)$$

Then, substituting q_c in the previous equation leads to the expression:

$$\Delta E_{na}^\ddagger = (\lambda + \Delta E_{if})^2 / 4\lambda \text{ with } \lambda = 1/2f(q_i - q_f)^2 \quad (5)$$

where $\lambda = V_f(q_i) - V_f(q_f)$ is the reorganization energy (see figure S1).

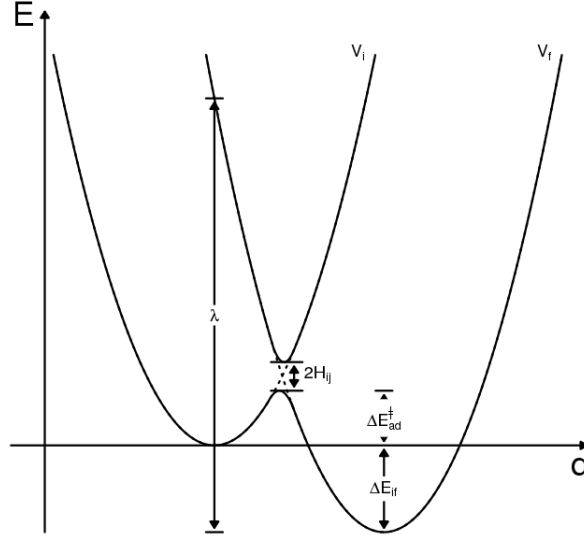


Figure S1: Adiabatic and non-adiabatic curves for an asymmetric electron transfer reaction.

When the initial and final electronic states interact significantly, they will be coupled by the Hamiltonian matrix element $H_{if} = H_{fi}$. This coupling is assumed to be independent of q . In the limit of slow nuclear motions, the so-called adiabatic (ad) potential energy curves, $W_{\pm}(q)$, are obtained by solving the secular equation:

$$\begin{vmatrix} V_i(q) - W_{\pm}(q) & H_{if} \\ H_{if} & V_f(q) - W_{\pm}(q) \end{vmatrix} = 0. \quad (6)$$

This leads to the following polynomial equation:

$$(1/2fQ_i^2 - W_{\pm})(1/2fQ_f^2 + \Delta E_{if} - W_{\pm}) - H_{if}^2 = 0 \quad (7)$$

$$\text{with } Q_i = q - q_i \text{ and } Q_f = q - q_f$$

To find the expression of the adiabatic free energy barrier, equation (7) has been solved at the initial (q_i) and transition (q_c) state geometries, assuming that their position is unchanged on going from the diabatic to the adiabatic states. First, one can demonstrate that the discriminant of the previous polynomial can be written as:

$$D = (1/2f(Q_i^2 - Q_f^2) - \Delta E_{if})^2 + H_{if}^2 \quad (8)$$

1) At the initial state geometry ($Q_i = 0$ and $Q_f = q_i - q_f$) the discriminant simplifies to:

$$D = (\lambda + \Delta E_{if})^2 + 4H_{if}^2 \quad (9)$$

and the adiabatic potential energies at this point are:

$$W_{\pm} = \frac{\lambda + \Delta E_{if}}{2} \pm \sqrt{\frac{(\lambda + \Delta E_{if})^2}{4} + H_{if}^2} \quad (10)$$

2) At the crossing point ($q = q_c$) we can write:

$$Q_i = \frac{\Delta E_{if} + \lambda}{f(q_f - q_i)} \quad Q_f = \frac{\Delta E_{if} - \lambda}{f(q_f - q_i)} \quad (11)$$

and then:

$$1/2f (Q_i^2 - Q_f^2) = \Delta E_{if} \quad 1/2f (Q_i^2 + Q_f^2) = \frac{\Delta E_{if}^2 + \lambda^2}{2\lambda} \quad (12)$$

At this point the discriminant is $D = 4H_{if}^2$ and the adiabatic potential energies are:

$$W_{\pm} = \frac{(\lambda + \Delta E_{if})^2}{4\lambda} \pm H_{if} = \Delta E_{na}^{\ddagger} \pm H_{if}. \quad (13)$$

Finally, we can determine the adiabatic free energy barrier by calculating the difference between the transition state and initial energies:

$$\Delta E_{ad}^{\ddagger} = W_-(q_c) - W_-(q_i) = \Delta E_{na}^{\ddagger} - \Delta \quad (14)$$

with $\Delta = H_{if} + \frac{\lambda + \Delta E_{if}}{2} - \sqrt{\frac{(\lambda + \Delta E_{if})^2}{4} + H_{if}^2}$

2 Electron transfer rates

The rate constant for electron transfer in the semi-classical approximation (k_{sc} , referred as the Landau-Zener or LZ rate in the main article) can be related to the classical rate constant k_{cl} by introducing a thermally averaged electronic transmission coefficient κ_{el} and the nuclear tunneling factor Γ_n ($\kappa_{el} = 1 \Rightarrow$ adiabatic, $\kappa_{el} \neq 1 \Rightarrow$ non-adiabatic; $\Gamma_n = 1 \Rightarrow$ no tunneling effects, $\Gamma_n \neq 1 \Rightarrow$ tunneling effects) [1]:

$$k_{LZ} = k_{sc} = \kappa_{el} \Gamma_n k_{cl} \quad (15)$$

$$k_{cl} = \nu_{eff} \exp \{ -\beta (\Delta E_{na}^{\ddagger} - \Delta) \} \quad (16)$$

where ν_{eff} is the frequency along the reaction coordinate. The electronic transmission is given by:

$$\kappa_{el} = \frac{2P_{LZ}}{1 + P_{LZ}} \quad (17)$$

$$P_{LZ} = 1 - \exp(-2\pi\gamma) \quad (18)$$

$$2\pi\gamma = \frac{\pi^{3/2} |H_{if}|^2}{h\nu_{eff} \sqrt{\lambda k_B T}} \quad (19)$$

where P_{LZ} is the Landau-Zener transition probability for a single surface crossing event. The parameter $2\pi\gamma$ determines the adiabaticity of the reaction. If $2\pi\gamma \ll 1$ the reaction is non-adiabatic and the exponent in equation (18) can be expanded in a Taylor series and truncated after the first order term, giving $P_{LZ} = 2\pi\gamma$ and $\kappa_{el} = 2P_{LZ}$. Insertion

of this result into equation 15 and assuming that $\lambda + \Delta E_{if} \gg |H_{if}|$ ($\Delta \approx 0$) gives the non-adiabatic (or Marcus) ET rate [1, 2, 3]:

$$k_{Marcus} = \frac{2\pi}{\hbar} |H_{if}|^2 \sqrt{\frac{1}{4\pi\lambda k_B T}} \exp(-\beta\Delta E_{na}^\ddagger) \quad (20)$$

In the opposite limit $2\pi\gamma \gg 1$, the ET is adiabatic and P_{LZ} and κ_{el} approach unity. The rate expression is the same as for “standard” chemical reactions in the classical transition state approximation $k_{ad} = k_{cl}$ [2].

On the other hand, a full quantum-mechanical treatment of non-adiabatic transitions, based upon Fermi’s golden rule, leads to the Marcus-Levich-Jortner (MLJ) rate equation:

$$k_{MLJ} = \frac{2\pi}{\hbar} |H_{if}|^2 \sqrt{\frac{1}{4\pi\lambda_s k_B T}} \sum_{n=0}^{\infty} \exp(-S_{eff}) \frac{S_{eff}^n}{n!} \exp\left\{-\frac{(\Delta E_{if} + \lambda_s + n\hbar\omega_{eff})^2}{4\lambda_s k_B T}\right\} \quad (21)$$

with $\lambda_i = \hbar\nu_{eff}S_{eff} = \hbar\omega_{eff}S_{eff}$, which turns out [1, 4, 5, 6] to be equivalent to the Marcus expression in the case of an ET reaction driven by solvent coordinates [7].

The evolution of the Marcus, MLJ and LZ rate expressions as a function of the site energy difference and the electronic coupling can be compared on Figure S2. Notice the similarity between the LZ and the Marcus rates, as the latter is the non-adiabatic limit of the former, and how different is the contour map of the MLJ expression in comparison with the other two.

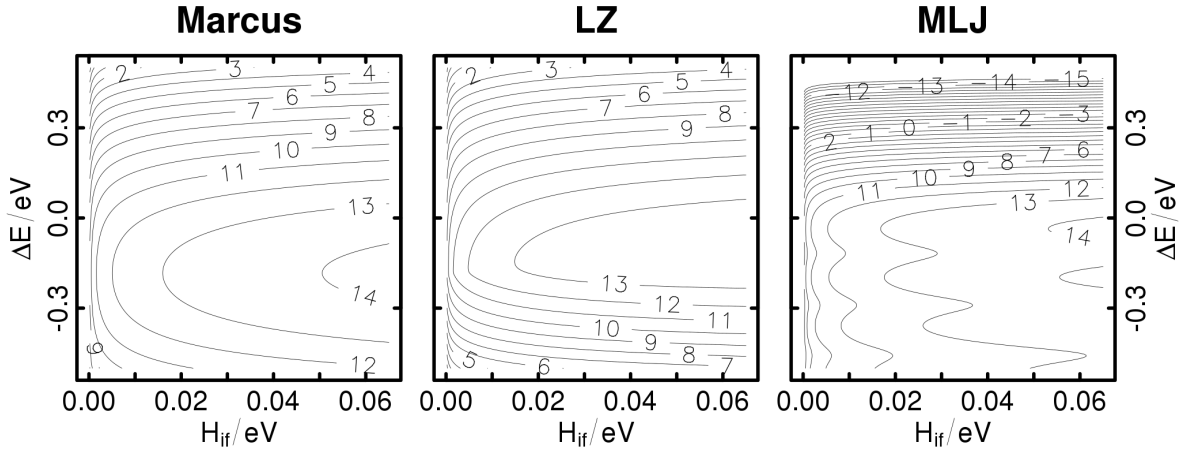


Figure S2: Contour plots of the decimal logarithm of the Marcus (left), LZ (Middle) and MLJ (right) rate expressions as a function of the site energy difference and the electronic coupling, setting the reorganization energies ($\lambda_i = 0.147$ eV and $\lambda_s = 0.036$ eV) and effective mode frequency ($\hbar\nu_{eff} = 0.179$ eV) to the values calculated for PCBM.

3 Reorganization energies

Hung-Rhys (HR) factors were obtained from the dimensionless displacement parameters B_j usually employed in the evaluation of the Franck-Condon (FC) vibronic progressions in electronic spectra [8]. The latter, assuming the harmonic approximation, are defined as:

$$B_j = \sqrt{\frac{\nu_j}{h}} (X_K - X_H) M^{1/2} L_j(K) \quad (22)$$

where $X_{K,H}$ are the $3N$ dimensional vectors of the equilibrium Cartesian coordinates of the K, H^{th} state (here the neutral and negative molecular states), M is the $3N \times 3N$ diagonal matrix of the atomic masses, and $L_j(K)$ is the $3N$ vector describing the normal coordinate Q_j of the K state in terms of mass-weighted Cartesian coordinates. The HR factors were evaluated from:

$$S_j = \frac{1}{2} B_j^2 \quad (23)$$

Table S1: Huang-Rhys factors for C₆₀, PCBM and ThCBM (only $S_j > 0.005$ are reported)

C ₆₀		PCBM		ThCBM	
ν_{eff}/cm^{-1}	S_j	ν_{eff}/cm^{-1}	S_j	ν_{eff}/cm^{-1}	S_j
300.3	0.0062	14.0	0.3072	13.8	0.2034
312.9	0.0688	18.6	0.1790	19.4	0.5953
430.1	0.0067	23.1	0.1821	24.1	0.2383
484.8	0.0056	42.0	0.0688	42.0	0.1571
486.6	0.0235	46.8	0.0177	58.0	0.0223
495.6	0.0068	53.5	0.0106	63.6	0.0081
564.8	0.0056	66.7	0.0136	98.7	0.0054
576.1	0.0139	105.0	0.0184	106.3	0.0674
705.3	0.0072	107.2	0.0214	177.1	0.0075
709.4	0.0113	128.5	0.0071	206.7	0.0191
730.0	0.0345	210.0	0.0146	240.7	0.0061
764.4	0.0164	272.3	0.0181	254.4	0.0052
783.6	0.0256	282.8	0.0154	263.8	0.0053
802.2	0.0640	300.5	0.0191	266.5	0.0187
837.7	0.0289	428.5	0.0855	285.0	0.0155
838.1	0.0241	436.2	0.0477	307.4	0.0185
1017.7	0.0392	455.1	0.0201	429.2	0.0948
1128.5	0.0505	486.6	0.0154	437.5	0.0328
1200.5	0.0169	488.7	0.0147	455.6	0.0243
1292.1	0.0133	540.0	0.0172	487.7	0.0227
1308.5	0.0065	704.8	0.0486	489.8	0.0070
1363.4	0.0101	706.6	0.0094	543.3	0.0167
1435.5	0.0087	706.8	0.0162	706.6	0.0122
1543.6	0.0386	714.4	0.0075	707.7	0.0451
1597.3	0.0091	721.1	0.0300	709.0	0.0453
1603.5	0.0200	732.1	0.0071	710.6	0.0073
		755.9	0.0149	722.9	0.0434
		767.1	0.0123	723.8	0.0096
		903.7	0.1203	732.3	0.0053
		908.8	0.0093	733.2	0.0057
		1132.6	0.0119	753.9	0.0079
		1221.8	0.0259	767.0	0.0162
		1222.2	0.0057	900.2	0.0383
		1274.3	0.0054	902.6	0.2838
		1454.8	0.0442	1032.7	0.0060
		1457.4	0.0074	1131.5	0.0127
		1490.8	0.0943	1222.4	0.0696
		1491.0	0.0055	1454.5	0.0458
		1492.8	0.0145	1457.4	0.0066
		1596.0	0.0165	1490.7	0.0955
		1601.8	0.0255	1492.7	0.0399
		1826.4	0.0667	1596.0	0.0148
		3067.2	0.0100	1601.7	0.0269
		3068.0	0.0495	1827.5	0.1667
				3067.9	0.1472
				3068.9	0.0198

4 Electronic properties

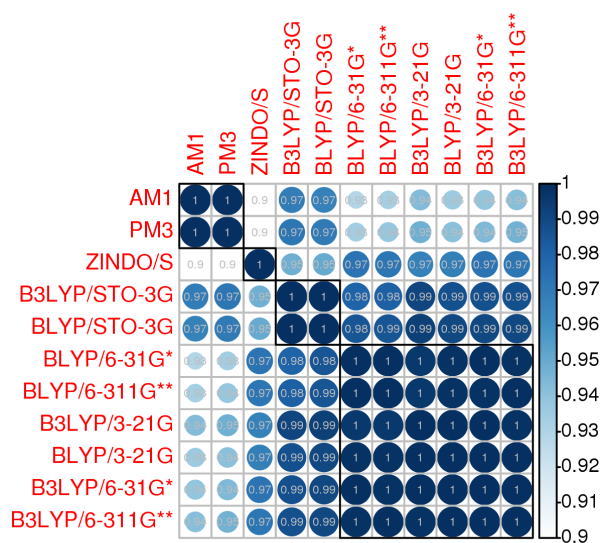


Figure S3: Correlation diagram of the site energies calculated between the L0, L1 and L2 orbitals of 7 different PCBM dimers at different DFT and semi-empirical levels.

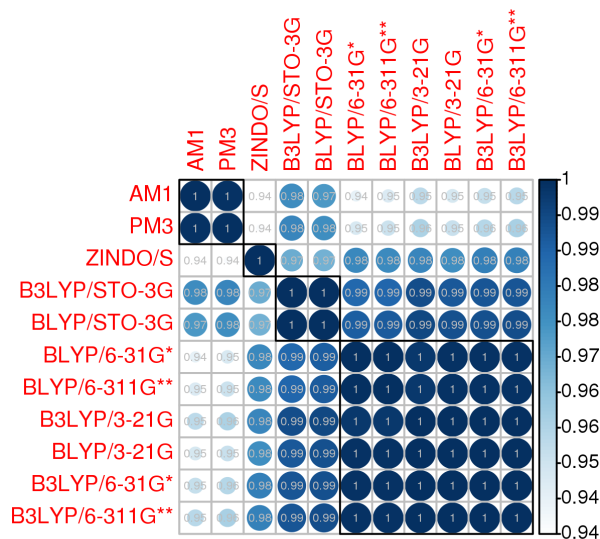


Figure S4: Correlation diagram of the site energy differences calculated between the L0, L1 and L2 orbitals of 7 different PCBM dimers at different DFT and semi-empirical levels.

5 Results for the Marcus and MLJ rate expressions

The ET rates forming the F1-networks calculated with the Marcus and MLJ expressions are reported in Figures S5 and S6. Like those from the LZ expression which are plotted in the main text, they are represented by cones whose basis areas are proportional to the rates. As the LZ, Marcus and MLJ expressions can sometimes furnish ET rates differing by orders of magnitude, different scaling factors have been used to represent these three sets of data. Despite this difference in the representations of the rates in Figures 6, S5 and S6, we can clearly notice the good qualitative agreement of the results provided by the three expressions. Only a small disagreement can be noticed in the size of the cones for some particularly asymmetric pathways defined between non-equivalent sites in the triclinic structures. These differences can be rationalized by carefully analysing the position of these pathways on the maps of the LZ, Marcus and MLJ rates in Figure S2.

Figures S7 and S8 represent the effective hopping probabilities resulting from our KMC simulations performed on the Marcus and MLJ F1-networks. Those for the simulations including the L1 and L2 orbitals (F3-network) are given in Figures S9 and S10. Again, the agreement between the results obtained with the three rate expressions is evident. The dimensionality and main transport directions of the F1- and F3-networks found with the LZ expression are retained when using the Marcus or MLJ ones. The mobility tensors obtained from these KMC simulations are compiled in Tables S2 (Marcus) and S3 (MLJ). They are also represented by ellipsoids in Figures S7, S8, S9 and S10. The Marcus and MLJ mobilities are respectively lower ($\mu_{Marcus} \sim 0.75\mu_{LZ}$) and higher ($\mu_{MLJ} \sim 3\mu_{LZ}$) than those obtained with the LZ expression. This can be explained by the fact that electron transport is globally dominated by L0L0 transitions ($\Delta E_{L0L0} = 0$), for which we always have $k_{Marcus} < k_{LZ} < k_{MLJ}$ in the range of our electronic couplings ($J < 65$ meV).

Finally, Figures S11, S12 and S13 report histograms of the ET rates for all the crystal structures, respectively calculated with the LZ, Marcus and MLJ expressions. These have been decomposed according to the different molecular orbital contributions. For the PCBM/DCM and PCBM/CS₂ structures, the separation between the distributions of the rates forming the F1-network (L0L0 transitions) and those allowing to escape it, which was observed for the LZ expression in the main text, is also visible for the other two expressions. This confirmed the insensitivity of these two structures to the inclusion of the L1 and L2 orbitals in the percolation network. Notice for the MLJ expression that the endothermal transitions can display extremely small ET rates (lower than $1s^{-1}$). This is consistent with the landscape of the map of the MLJ expression in Figure S2 which abruptly decrease when ΔE increases, in the region of $\Delta E > 0$. The main difference between Figures S11 and S12 is that the Marcus expression provides higher ET rates for strongly exothermal transitions (L2L0). Again, this is consistent with the maps in Figure S2, which show that the Marcus ET rates are always larger than the LZ ones when $\Delta E < -0.18$ eV.

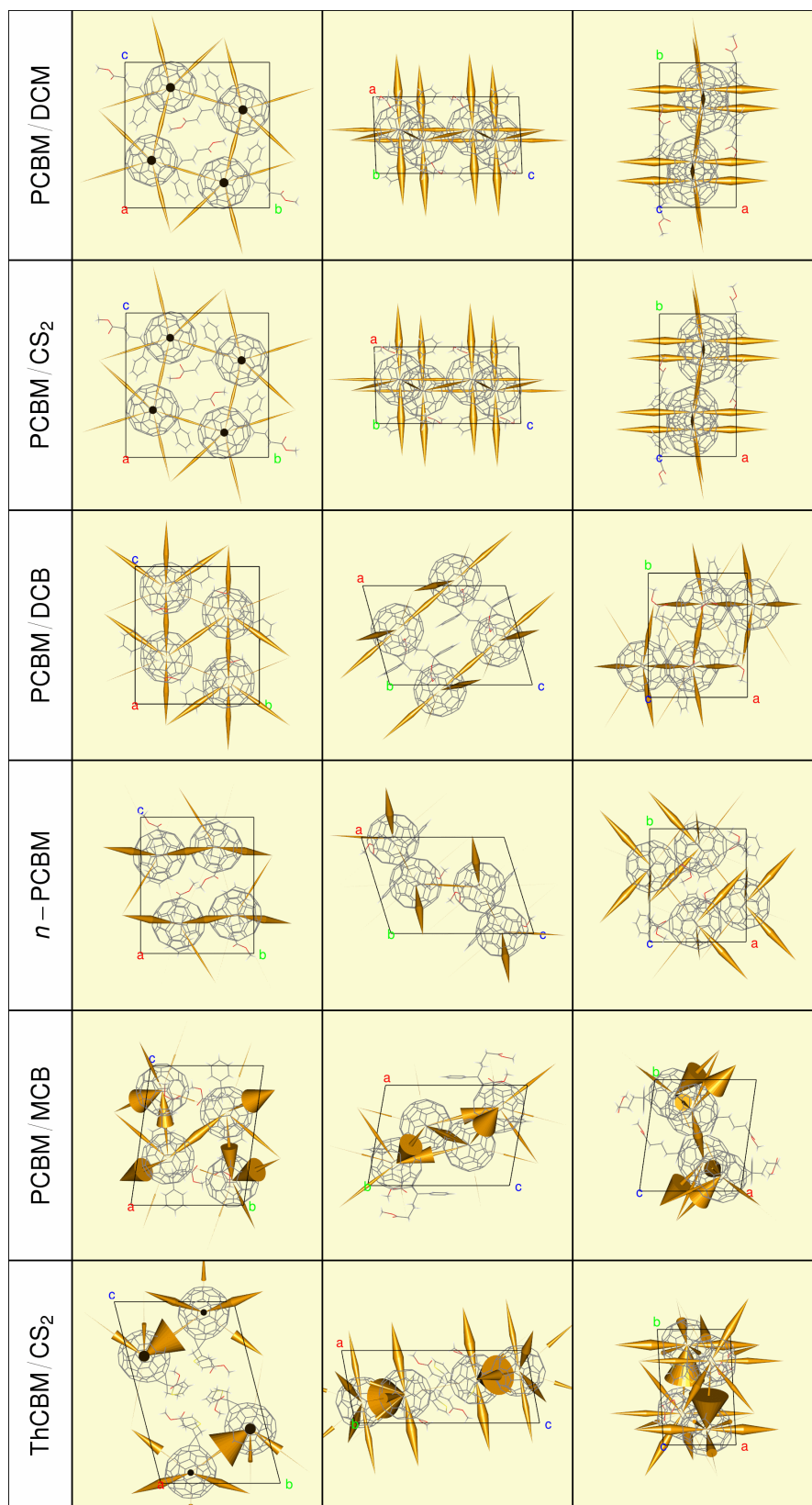


Figure S5: Representation of the Marcus ET rates for the L0L0 transitions (cones with bases proportional to the rates, pointing towards the destination fullerene), forming the F1-networks.

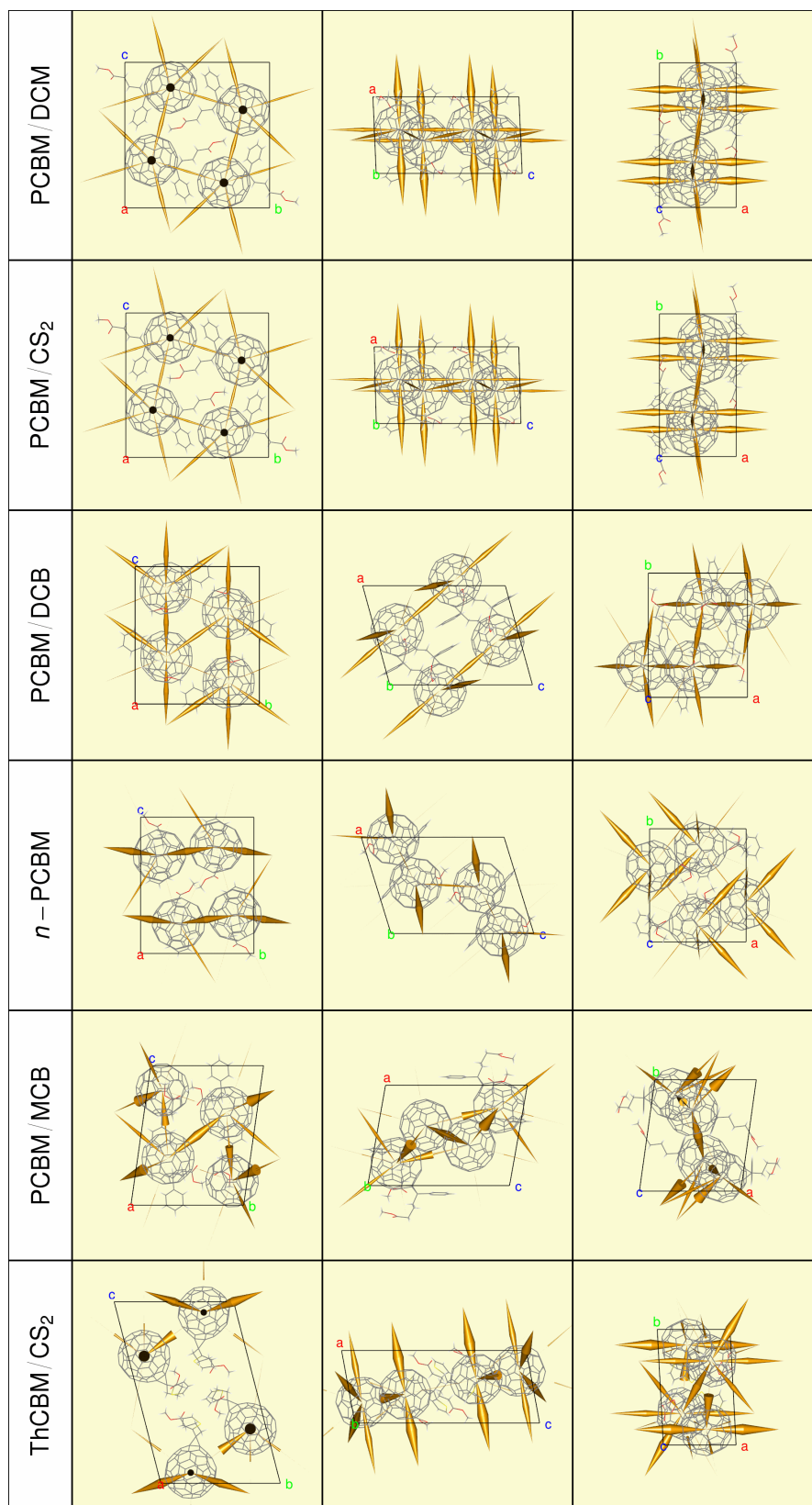


Figure S6: Representation of the MLJ ET rates for the L0L0 transitions (cones with bases proportional to the rates, pointing towards the destination fullerene), forming the F1-networks.

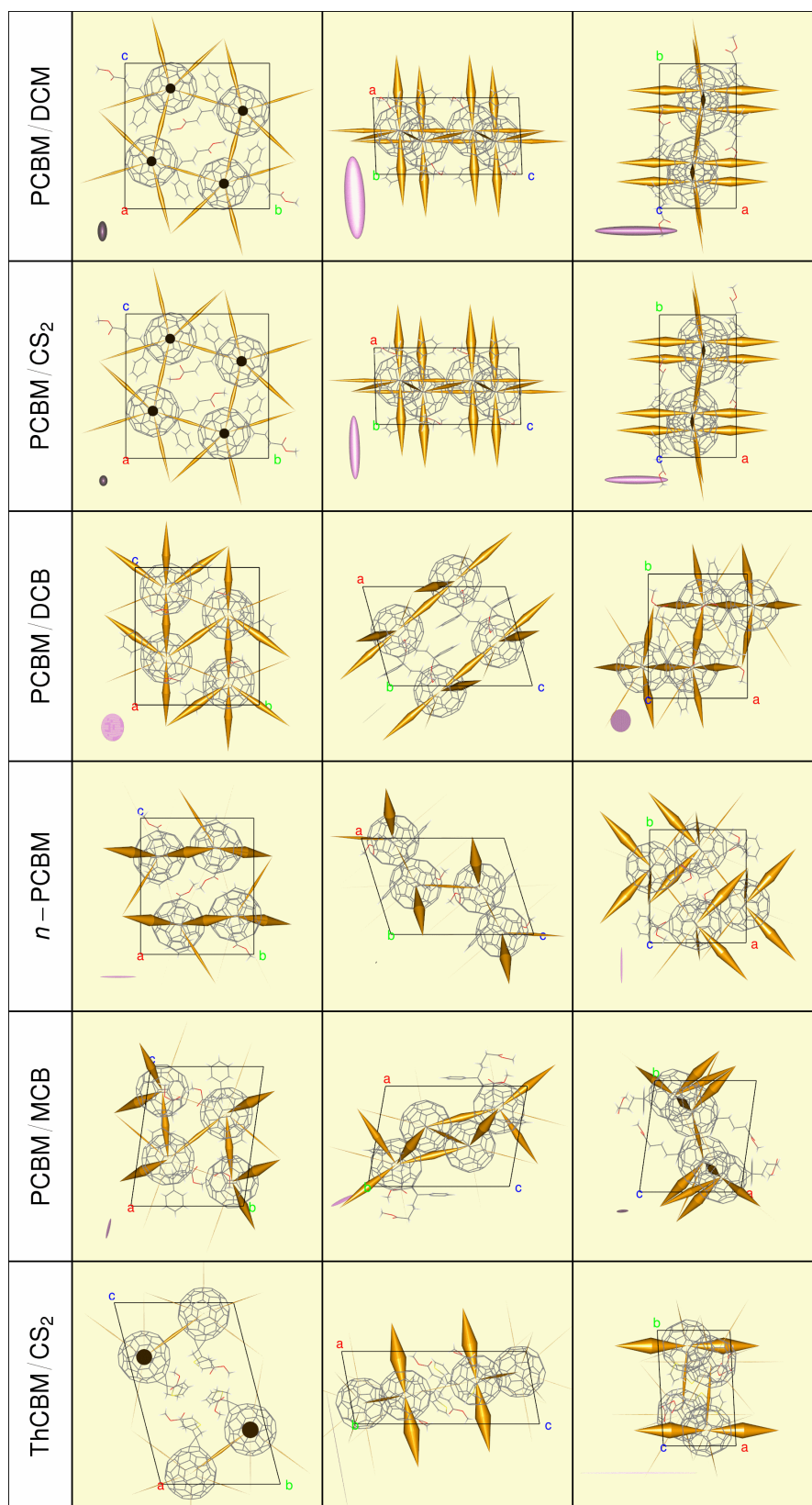


Figure S7: Effective hopping probabilities (cones) and associated mobility tensors (ellipsoids) within the F1-networks, obtained for the Marcus expression.

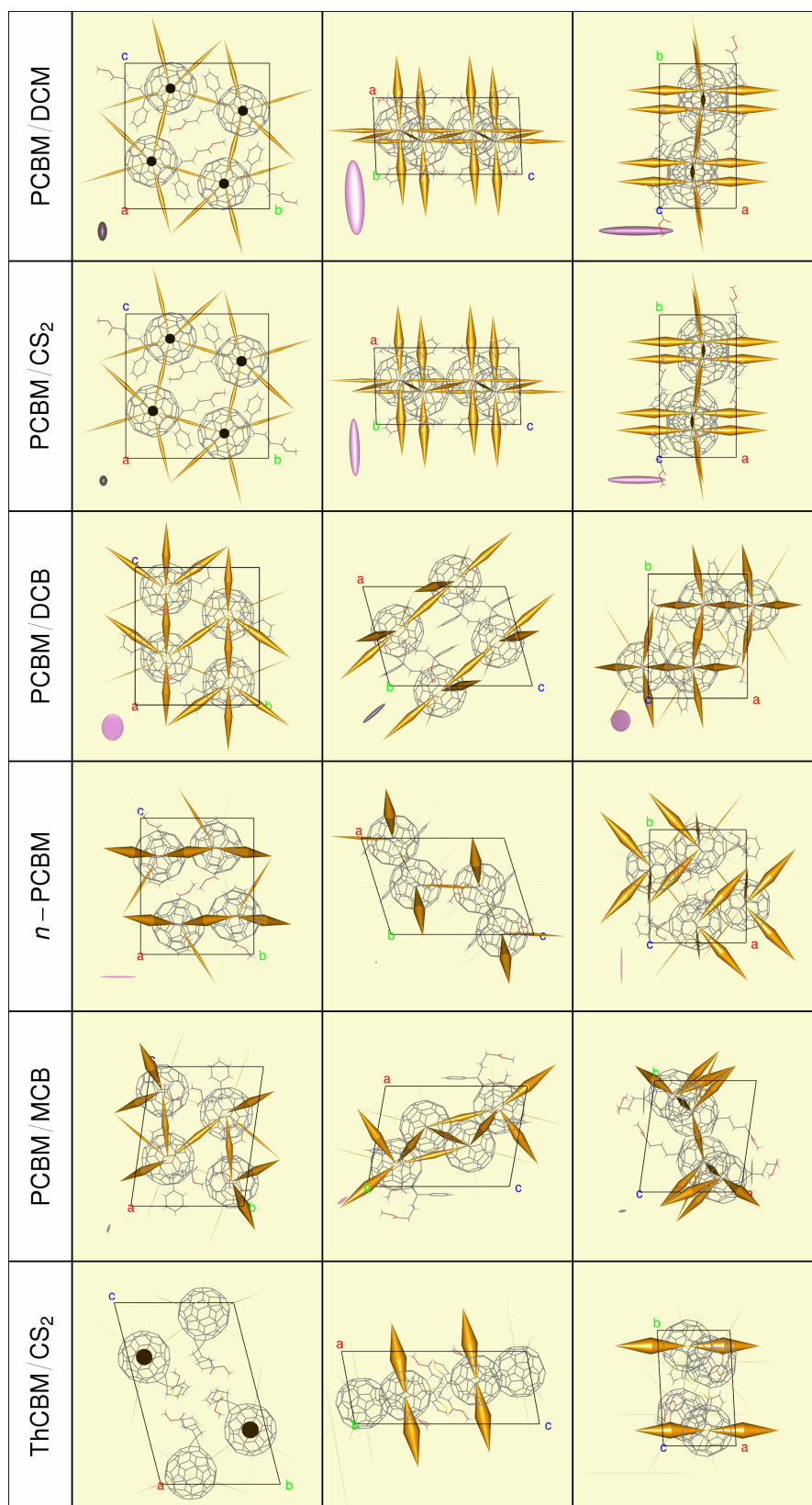


Figure S8: Effective hopping probabilities (cones) and associated mobility tensors (ellipsoids) within the F1-networks, obtained for the MLJ expression.

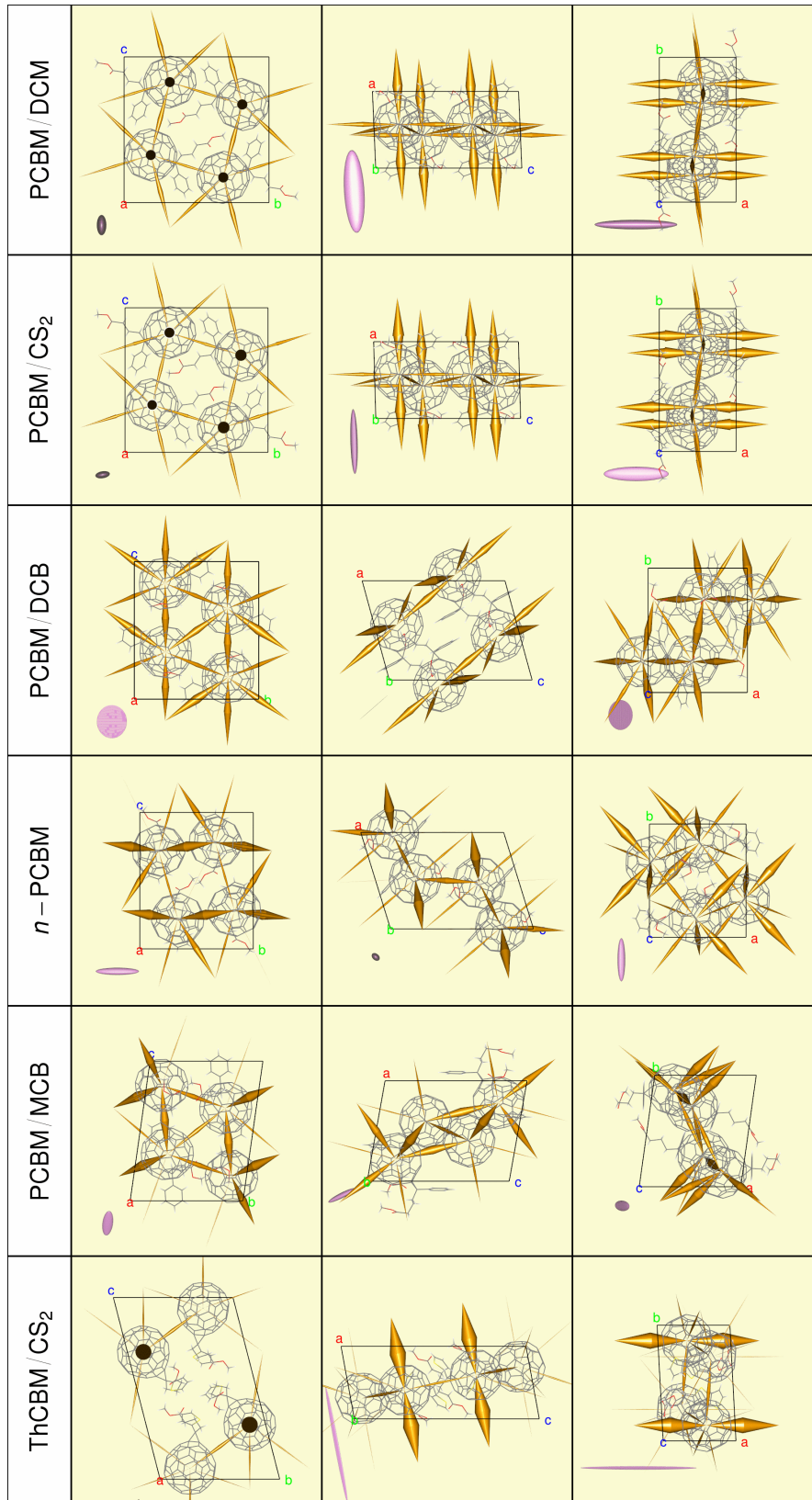


Figure S9: Effective hopping probabilities (cones) and associated mobility tensors (ellipsoids) within the F3-networks, obtained from the Marcus expression.

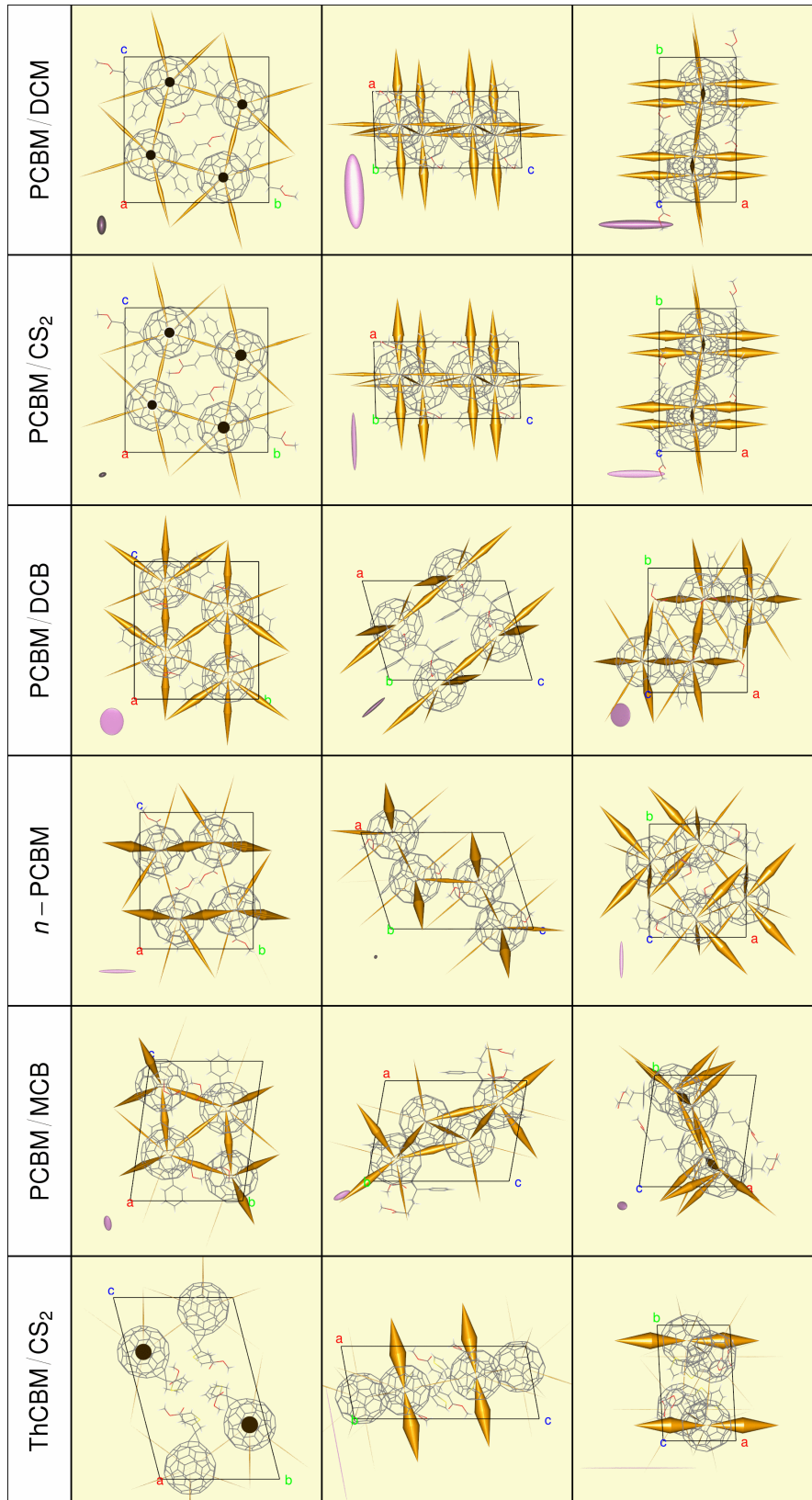


Figure S10: Effective hopping probabilities (cones) and associated mobility tensors (ellipsoids) within the F3-networks, obtained from the MLJ expression.

PCBM/DCM					PCBM/CS ₂				
	Eigenvalues	Eigenvectors			Eigenvalues	Eigenvectors			
		x	y	z		x	y	z	
F1	0.69	-1.00	0.00	0.01	F1	0.53	-1.00	0.00	0.01
	0.17	0.01	0.00	1.00		0.09	0.01	0.01	1.00
	0.08	0.00	-1.00	0.00		0.07	0.00	-1.00	0.01
F3	0.69	-1.00	0.00	0.01	F3	0.54	1.00	0.00	0.00
	0.17	-0.01	0.00	-1.00		0.12	0.00	0.98	0.19
	0.08	0.00	1.00	0.00		0.05	0.00	-0.13	0.99
PCBM/DCB					<i>n</i> -PCBM				
	Eigenvalues	Eigenvectors			Eigenvalues	Eigenvectors			
		x	y	z		x	y	z	
F1	0.25	-0.43	0.00	-0.90	F1	0.30	0.00	1.00	0.00
	0.19	0.00	-1.00	0.00		0.02	-0.62	0.00	-0.79
	0.00	0.90	0.00	-0.43		0.01	-0.76	0.00	0.65
F3	0.30	0.43	0.00	0.90	F3	0.36	0.00	-1.00	0.00
	0.25	0.00	1.00	0.00		0.08	0.83	0.00	-0.55
	0.00	0.91	0.00	-0.42		0.06	-0.53	0.00	-0.85
PCBM/MCB					ThCBM/CS ₂				
	Eigenvalues	Eigenvectors			Eigenvalues	Eigenvectors			
		x	y	z		x	y	z	
F1	0.22	0.62	0.18	0.76	F1	1.00	1.00	0.00	0.00
	0.04	0.80	-0.06	-0.60		0.01	0.00	-0.99	-0.16
	0.03	0.04	-0.98	0.17		0.00	0.00	-0.18	0.98
F3	0.25	0.60	0.12	0.79	F3	0.99	1.00	0.00	0.00
	0.09	-0.07	-0.98	0.18		0.04	0.00	-0.50	-0.87
	0.06	0.81	-0.16	-0.57		0.01	0.00	-0.90	0.44
R1	0.05	1.00	0.00	0.00	R1	0.95	1.00	0.00	0.00
	0.00	0.01	1.00	0.00		0.00	0.00	-0.18	-0.98
	0.00	0.00	0.95	0.30		0.00	0.00	-0.50	0.87
R3	0.06	1.00	0.00	0.00	R3	0.95	1.00	0.00	0.00
	0.00	0.01	1.00	0.00		0.00	0.00	-0.18	-0.98
	0.00	0.00	0.84	0.55		0.00	0.00	-0.39	0.92

Table S2: Eigenvalues ($\text{cm}^2\text{V}^{-1}\text{s}^{-1}$) and eigenvectors of the mobility tensors calculated considering either the F1-, F3-, R1- or R3-networks (using the Marcus rates) for each crystal structure.

PCBM/DCM					PCBM/CS ₂				
	Eigenvalues	Eigenvectors			Eigenvalues	Eigenvectors			
		x	y	z		x	y	z	
F1	2.09	-1.00	0.00	0.02	1.61	-1.00	0.00	0.01	
	0.54	0.02	0.00	1.00	0.29	0.01	0.02	1.00	
	0.26	0.00	-1.00	0.00	0.22	0.00	-1.00	0.02	
F3	2.09	-1.00	0.00	0.02	1.61	1.00	0.00	-0.01	
	0.54	0.02	0.00	1.00	0.23	0.00	0.91	0.41	
	0.26	0.00	-1.00	0.00	0.12	0.00	-0.31	0.95	
PCBM/DCB					<i>n</i> -PCBM				
	Eigenvalues	Eigenvectors			Eigenvalues	Eigenvectors			
		x	y	z		x	y	z	
F1	0.83	-0.43	0.00	-0.90	1.01	0.00	1.00	0.00	
	0.61	0.00	-1.00	0.00	0.07	-0.62	0.00	-0.79	
	0.00	0.88	0.00	-0.48	0.02	-0.73	0.00	0.68	
F3	0.85	0.43	0.00	0.90	1.03	0.00	1.00	0.00	
	0.66	0.00	1.00	0.00	0.12	-0.69	0.00	-0.73	
	0.00	0.88	0.00	-0.47	0.09	-0.71	0.00	0.70	
PCBM/MCB					ThCBM/CS ₂				
	Eigenvalues	Eigenvectors			Eigenvalues	Eigenvectors			
		x	y	z		x	y	z	
F1	0.36	0.76	0.22	0.62	3.33	1.00	0.00	0.00	
	0.11	0.70	-0.10	-0.71	0.01	0.00	-0.73	-0.68	
	0.07	-0.06	-0.93	0.36	0.00	0.00	-0.57	0.82	
F3	0.50	-0.63	0.08	-0.78	3.32	1.00	0.00	0.00	
	0.23	-0.32	-0.91	0.24	0.03	0.00	0.54	0.84	
	0.19	-0.60	0.67	0.43	0.01	0.00	-0.85	0.53	
R1	0.18	1.00	0.00	0.00	3.26	-1.00	0.00	0.00	
	0.00	0.01	1.00	0.00	0.00	0.00	0.18	0.98	
	0.00	0.00	0.83	0.56	0.00	0.00	-0.87	0.49	
R3	0.20	1.00	0.00	0.00	3.24	1.00	0.00	0.00	
	0.00	0.01	1.00	0.00	0.00	0.00	-0.18	-0.98	
	0.00	-0.03	-0.49	0.87	0.00	0.00	-0.98	0.22	

Table S3: Eigenvalues ($\text{cm}^2\text{V}^{-1}\text{s}^{-1}$) and eigenvectors of the mobility tensors calculated considering either the F1-, F3-, R1- or R3-networks (using the MLJ rates) for each crystal structure.

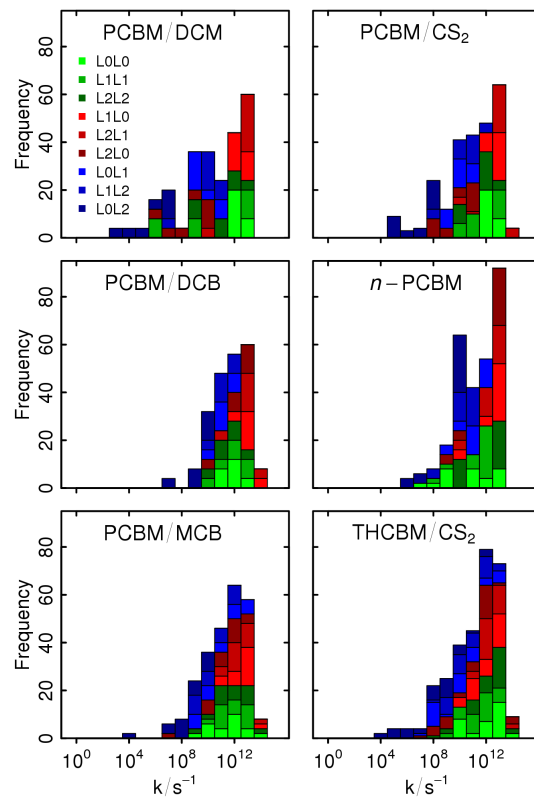


Figure S11: Decomposition by molecular orbital contributions of the LZ rates distributions of the different crystal structures. Green, blue and red bins are respectively the contributions of flat, upward, and downward ETs.

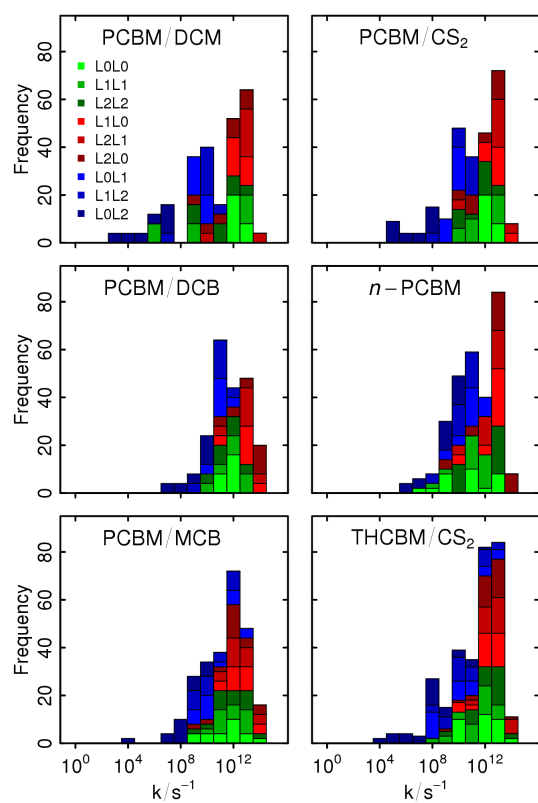


Figure S12: Decomposition by molecular orbital contributions of the Marcus rates distributions of the different crystal structures. Green, blue and red bins are respectively the contributions of flat, upward, and downward ETs.

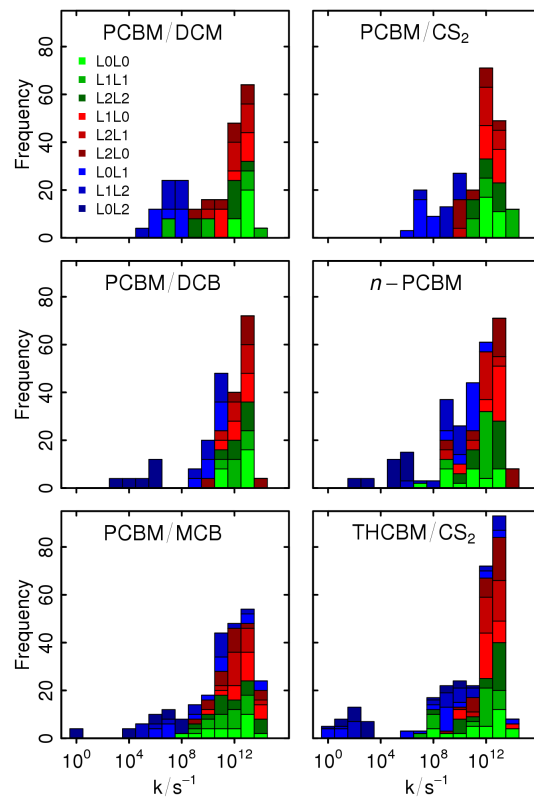


Figure S13: Decomposition by molecular orbital contributions of the MLJ ET rates distributions of the different crystal structures. Green, blue and red bins are respectively the contributions of flat, upward, and downward ETs.

6 Electric field dependency

We performed additional KMC simulations on the F1-network (LOLO transitions only) of the PCBM/CS₂ structure, changing the norm of the applied electric field (F). F was applied along the main direction of the mobility tensor reported in our paper ([100], x -axis) and scanned over the range 10^4 - 10^7 V cm⁻¹. We monitored the evolution of the average (over 16 different KMC simulations) ET rates, the number of hopping events along F and its opposite direction $\bar{[100]}$, as well as the x -, y - and z -components of the drift distance and velocity. These results are reported in Figure S14.

As expected for the transport of negatively charged electrons, the ET rate in the direction of the electric field ([100]) decreases when its norm increases, while in the opposite direction ($\bar{[100]}$) it first increases and then decreases once the inverted region of the rate expression is reached (after $4 \cdot 10^6$ V cm⁻¹). The average of all the other ET rates within the structure is also reported in Figure S14 (green line). As these rates belong to a plane nearly perpendicular to the electric field direction, their average is not very sensitive to the increase in F . Despite this low sensitivity, these rates enter in competition with the [100] and $\bar{[100]}$ rates when F becomes higher than $\sim 3 \cdot 10^6$ and $\sim 8 \cdot 10^6$ V cm⁻¹, respectively. This competition is at the origin of the sensitivity of the average number of hopping events in that plane, when F becomes higher than $3 \cdot 10^6$ V cm⁻¹. At low electric fields this number is non-negligible, indicating that the charge spends appreciable time diffusing in this plane during its global drift along the $\bar{[100]}$ direction. At very high electric field (10^7 V cm⁻¹), the charge hops exclusively in this plane.

The plots of the drift distance confirm that the electron drifts in the direction opposite to the electric field. Indeed, the main component of the drift distance is the x -component, which is always negative ($dx < 0$). At low electric fields, the charge performs a random walk about its starting position, leading to a null drift distance. When we increase the electric field, dx follow the evolution of the $\bar{[100]}$ rate. At very high electric fields (10^7 V · cm⁻¹), dz becomes non-negligible while dy stays null. This is due to the fact that the electron is confined in a plane which is almost but not perfectly orthogonal to F (in the PCBM/CS₂ structure, $\alpha = 90^\circ$, $\beta = 91.62^\circ$ and $\gamma = 90^\circ$). Overall, the drift velocity follows the same trend as the drift distance.

Using the previous results, the electron mobility has been evaluated along the electric field direction as: $\mu(F) = |V_x(F)|/F$. Looking at this expression, the evolution of $\mu(F)$ is given by the product of two functions: the drift velocity ($|V_x(F)|$) and the inverse of the electric field ($1/F$). Depending on the evolution of these two functions, the resulting mobility may increase or decrease. In our case, as the inverted region of the rate expression is reached at $4 \cdot 10^6$ V · cm⁻¹, a region where the $1/F$ function is still decreasing very abruptly, $\mu(F)$ decreases with F (see Figure S15).

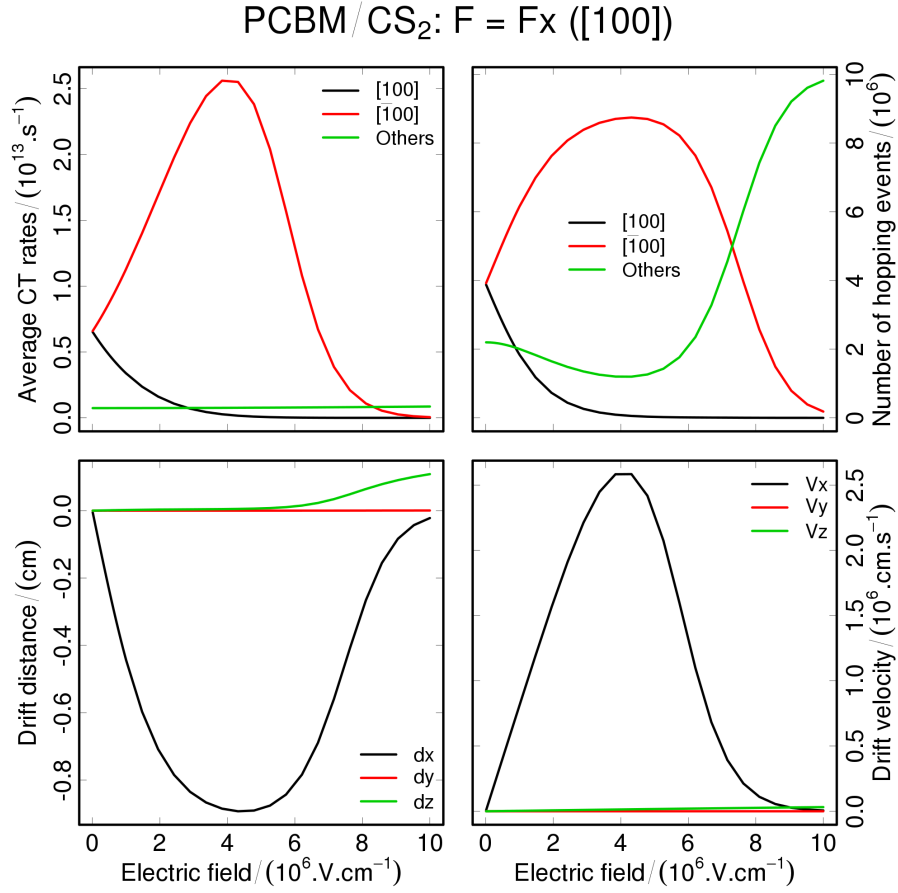


Figure S14: Evolution of the different outputs of the KMC simulations performed to compute the electron mobility as a function of the applied electric field.

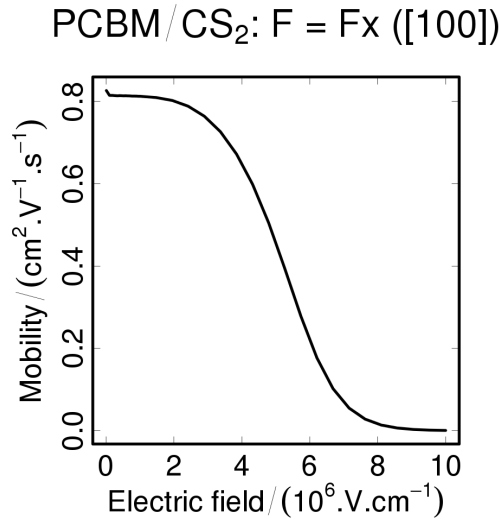


Figure S15: Electron mobility within the PCBM/CS₂ structure as a function of the applied electric field.

References

- [1] B. S. Brunschwig, J. Logan, M. D. Newton, and N. Sutin. A semiclassical treatment of electron-exchange reactions. application to the hexaaquoiron(ii)-hexaaquoiron(iii) system. *Journal of the American Chemical Society*, 102:5799–5809, 1980.
- [2] H. Oberhofer and J. Blumberger. Revisiting electronic couplings and incoherent hopping models for electron transport in crystalline c_{60} at ambient temperatures. *Physical Chemistry Chemical Physics*, 14:13846–13852, 2012.
- [3] R.A. Marcus. On the theory of oxidation-reduction reactions involving electron transfer. i. *Journal of Chemical Physics*, 24:966, 1956.
- [4] V. Rühle, A. Lukyanov, F. May, M. Schrader, T. Vehoff, J. Kirkpatrick, B. Baumeier, and D. Andrienko. Microscopic simulations of charge transport in disordered organic semiconductors. *Journal of Chemical Theory and Computation*, 7:3335–3345, 2011.
- [5] R.A. Marcus. Electron transfer reactions in chemistry. theory and experiment. *Reviews of Modern Physics*, 65:599, 1993.
- [6] R. Silbey, J. Jortner, S. A. Rice, and M. T. Vala Jr. Exchange effects on the electron and hole mobility in crystalline anthracene and naphthalene. *Journal of Chemical Physics*, 42:733, 1965.
- [7] *Chemical Dynamics in Condensed Phases*. Oxford University Press, 2006.
- [8] F. Negri and G. Orlandi. The t_1 resonance raman spectra of 1,3,5-hexatriene and its deuterated isotopomers: An *abinitio* re-investigation. *Journal of Chemical Physics*, 103:2412–2419, 1995.